1-1-2016

Compressive behavior of FRP-confined concrete-encased steel columns

Tao Yu
University of Wollongong, taoy@uow.edu.au

G Lin
Hong Kong Polytechnic University

Shi Shun Zhang
University of Wollongong, shishun@uow.edu.au

Compressive behavior of FRP-confined concrete-encased steel columns

Abstract

FRP-confined concrete-encased steel I-section columns (FCSCs) are an emerging form of hybrid columns. An FCSC consists of an outer FRP tube, an encased steel section and a concrete infill. The FCSCs possess many advantages over conventional reinforced concrete columns, including the excellent corrosion resistance, excellent ductility and ease for construction. Existing studies on FCSCs, however, have been rather limited. This paper presents a combined experimental and theoretical study on the behavior of FCSCs under concentric and eccentric compression. The experimental program included the testing of a total of 14 specimens, with the main variables being the section configuration, the thickness of the FRP tube and the loading scheme. The theoretical part included the development of a model for section analysis based on the so-called fiber element approach. The test results showed that the buckling of steel section was well constrained and the concrete was effectively confined in FCSCs, leading to a very ductile response under both concentric and eccentric compression. The theoretical model was shown to provide reasonably accurate predictions of the test results.

Keywords

concrete, encased, steel, columns, compressive, behavior, confined, frp

Disciplines

Engineering | Science and Technology Studies

Publication Details

Yu, T., Lin, G. & Zhang, S. S. (2016). Compressive behavior of FRP-confined concrete-encased steel columns. Composite Structures, 154 493-506.

COMPRESSIVE BEHAVIOR OF FRP-CONFINED CONCRETE-ENCASED STEEL COLUMNS

T. Yu[1*], G. Lin[2] and S.S. Zhang[3]

ABSTRACT: FRP-confined concrete-encased steel I-section columns (FCSCs) are an emerging form of hybrid columns. An FCSC consists of an outer FRP tube, an encased steel section and a concrete infill. The FCSCs possess many advantages over conventional reinforced concrete columns, including the excellent corrosion resistance, excellent ductility and ease for construction. Existing studies on FCSCs, however, have been rather limited. This paper presents a combined experimental and theoretical study on the behaviour of FCSCs under concentric and eccentric compression. The experimental program included the testing of a total of 14 specimens, with the main variables being the section configuration, the thickness of FRP tube and the loading scheme. The theoretical part included the development of a model for section analysis based on the so-called fiber element approach. The test results showed that the buckling of steel section was well constrained and the concrete was effectively confined in FCSCs, leading to a very ductile response under both concentric and eccentric compression. The theoretical model was shown to provide reasonably accurate predictions of the test results.

Keywords: FRP-confined concrete; FRP tube; Steel I-section; Concentric; Eccentric compression; Section analysis

[1] Senior Lecturer, School of Civil, Mining and Environmental Engineering, Faculty of Engineering and Information Sciences, University of Wollongong, Northfields Avenue, Wollongong, NSW 2522, Australia (Corresponding author). Tel: +61 2 4221 3786 Email: taoy@uow.edu.au
[2] PhD Candidate, Department of Civil and Environmental Engineering, The Hong Kong Polytechnic University, Hong Kong, China
[3] Lecturer, School of Civil, Mining and Environmental Engineering, Faculty of Engineering and Information Sciences, University of Wollongong, Northfields Avenue, Wollongong, NSW 2522, Australia

1 INTRODUCTION

In recent years, fiber-reinforced polymer (FRP) composites have found increasingly wide applications in civil engineering, both in the retrofit of existing structures and in new construction [1-4]. In particular, FRP has been widely accepted as an efficient confining material for concrete because of its high strength-to-weight ratio and tailorability in mechanical properties. The high strength-to-weight ratio translates into lighter/smaller components for installation, while the tailorability of FRP composites means that they can be designed to possess only a small axial stiffness so that their confinement effectiveness is not compromised by buckling due to substantial axial compressive stresses. Therefore, the use of FRP tubes as a confining device and a corrosion-resistant skin for concrete columns has been extensively explored for new construction [1,4]. Examples of FRP-confined concrete columns include (a) concrete-filled FRP tubes (CFFTs) with or without longitudinal reinforcement by steel bars (e.g., [5-11]); (b) hybrid FRP-concrete-steel double-skin tubular columns (DSTCs) (e.g., [1,12-16]) and (c) FRP-confined concrete-filled steel tubes (CCFTs) (e.g., [17-20]) (Fig. 1).

FRP-confined concrete-encased steel composite columns (FCSCs) are an emerging form of hybrid columns. The concept of FCSCs appears to be first explored by Liu *et al.* [21] as a rehabilitation technique for existing steel columns. Liu *et al.* [21] tested five FCSC specimens where FRP wraps were used and the steel sections in all specimens were notched to simulate the loss of section due to corrosion. Karimi and co-researchers [4,22,23] recently conducted experimental studies on the compressive behavior of FCSCs either using pre-fabricated FRP tubes for circular columns or FRP wraps for rectangular columns. Zakaib and Fam [24] conducted an experimental study on the flexural performance and moment connection of FCSCs with pre-fabricated FRP tubes. These studies have generally demonstrated the good performance of FCSCs and/or the use of FRP-confined concrete as an efficient method to retrofit/strengthen steel columns. The columns tested generally showed very ductile behavior.

In the existing studies, the pre-fabricated FRP tubes used typically had a significant longitudinal stiffness. However, an FRP tube containing fibres oriented close to the hoop direction appears much more attractive for FCSCs due to the following reasons: (a) the possibility and consequence of buckling of the FRP tube is avoided as it receives limited axial compressive stresses; (b) the FRP tube can be made thinner to minimise its cost; (c) the

presence of a steel section ensures a ductile response under bending-dominated loading, which makes the additional longitudinal reinforcement provided by the FRP tube unnecessary. The existing studies have also been generally limited to concentric axial compression tests of FCSCs, with little understanding on their behaviour under eccentric compression. Against this background, this paper presents a systematic experimental study on the compressive behavior of FCSCs. The experimental program included 14 column specimens tested under concentric or eccentric compression. Results from a theoretical model based on the section analysis method are also presented and compared with the test results.

2 EXPERIMENTAL PROGRAM

2.1 Specimen Details

In total, 14 column specimens were prepared and tested under concentric or eccentric compression, including nine circular specimens and five square specimens. All the circular specimens had a diameter of 203 mm, while all the square specimens had a side length of 200 mm and a corner radius of 25 mm (all values refer to the concrete core and do not include the thickness of the FRP tube). The specimens under concentric compression all had a height of 400 mm while those under eccentric compression all had a height of 600 mm. Besides the section shape, the main test variables included the load eccentricity (25 mm or 50 mm), the loading direction (bending about the major or the minor axis of the steel section) and the thickness of FRP tube [3.0 mm, 2.5mm, 1.5 mm or 0 (i.e., specimens without FRP tube)]. The details of all the specimens are summarized in Tables 1 and 2 for circular and square specimens respectively, while the dimensions of the steel I-sections, which were the same for all the specimens, are shown in Fig. 2.

Each specimen is given a name, which starts with a letter (“C” for circular or “S” for square), followed by a two-digit number which defines the load eccentricity, along with “Ma” standing for major axis or “Mi” for minor axis; this is then followed by a one or two-digit number to represent the thickness of FRP tube. For example, specimen “C-25Ma-3.0” is a circular specimen that was bent about the major axis of the steel I-section with a load eccentricity of 25 mm and confined with a 3.0-mm-thick FRP tube.

The preparation process of the test specimens included the following steps: (1) fabrication of the form, which consisted of an outer FRP tube or PVC tube (for specimens without an FRP

tube) and a steel I-section inside (Fig. 3a); strain gauges on the steel section were installed before the casting of concrete; (2) casting the concrete (Fig. 3b); (3) strengthening of both ends of the specimens using 25-mm-wide wet-layup FRP strips to avoid unexpected failure there (Fig. 3c); (4) installation of strain gauges on the FRP tube; and (5) capping of end surfaces of specimens with high-strength sulfur (Fig. 3d).

2.2 Material Properties

Standard tensile tests [25] of flat coupons, which were cut from different locations (i.e., the web, and the top and bottom flanges) of the steel I-section, were conducted to determine the material properties of steel. Typical stress-strain curves obtained from the coupon tests are shown in Fig. 4. The average values of the elastic modulus, yield stress, and tensile strength are 218.1 GPa, 321.7 MPa and 447.0 MPa with a standard deviation of 0.71 GPa, 12.4 MPa and 15.1 MPa respectively. In addition, two bare steel I-sections with a height of 400 mm and 600 mm respectively were tested under axial compression and the test results are presented later in the paper.

The circular GFRP tubes had an inner diameter of 203 mm and a thickness of 1.5 mm or 3.0 mm, while the square GFRP tubes had an inner sectional width of 200 mm, an inner corner radius of 25 mm and a thickness of 2.5 mm. The circular GFRP tubes were manufactured using a filament-winding process with the volume fraction of glass fiber being 59% and the angles of fibers being ±75° to the longitudinal axis of the tubes. These circular tubes had an elastic modulus of 33 GPa in the hoop direction according to the manufacturer. The square GFRP tubes were fabricated using a resin infusion process with 89% of fibers in the hoop direction and 11% of fibers in the longitudinal direction. Five coupons were cut from the square tubes, and were tested according to ASTM D3039 [26] to obtain the material properties in the hoop direction. The test results showed that the elastic modulus and the rupture strain in the hoop direction were 38 GPa and 0.0237 respectively. Although the circular and square GFRP tubes were formed via different processes, existing studies have shown that the behaviour of FRP-confined concrete depends mainly on the mechanical properties of the FRP tube in the hoop direction, and the effect of manufacturing method is negligible (e.g., [27]).

The concrete was cast in two batches (Batch 1 and Batch 2 in Tables 1 and 2). Three plain

concrete cylinders (150 mm × 300 mm) were tested for each batch to determine the concrete cylinder compressive strength. The average concrete strengths for Batch 1 and Batch 2 concrete obtained from these concrete cylinder tests are 24.9 MPa and 38.0 MPa with a standard deviation of 1.55 MPa and 1.87 MPa respectively.

2.3 Test Set-up and Instrumentation

For the steel I-section in each FCSC specimen, five axial strain gauges with a gauge length of 5 mm were installed at the mid-height (see Figs. 5a and 5b). For the GFRP tube in each FCSC specimen, six strain gauges with a gauge length of 20 mm were installed at the mid-height of the specimen, where four of the six strain gauges were in the hoop direction and the other two were in the axial direction (see Figs. 5a and 5b). For each bare steel I-section column, two axial strain gauges were installed at the mid-height (see Fig. 5c). The total axial shortening of all the specimens was measured with two linear variable displacement transducers (LVDTs) placed 180° apart from each other. For eccentrically-loaded specimens, an additional laser sensor was installed to measure the lateral deflection of the mid-height section.

All specimens were tested at the University of Wollongong using a Denison Compression Testing Machine with a load capacity of 5000 kN. The load was applied with displacement control at a loading rate of 0.3 mm/min for all specimens. For the eccentrically-loaded specimens, the load was applied through a steel roller at each end of the specimen so that the designed eccentricity could be accurately achieved (see Fig. 6b). All test data, including the strains, loads, and displacements, were recorded simultaneously by a data logger.

3 EXPERIMENTAL RESULTS

3.1 Failure Modes

The bare steel I-section columns failed by local buckling after yielding of steel (Fig. 7a). For the two hybrid columns without an FRP tube (i.e., specimens C-00-0 and S-00-0), concrete spalling occurred in a brittle manner, which was then followed by local buckling of the embedded steel section (Fig. 7b). All the FCSCs failed by rupture of the FRP tube due to hoop tension. The FRP rupture generally occurred in the mid-height region (Fig. 7c), and was localized at or close to one of the four rounded corners for the square specimens (Fig. 7d).

For eccentrically-loaded specimens, the FRP rupture occurred on the compression side because of the more pronounced lateral expansion of concrete there (Figs. 7e and 7f). After rupture of the FRP tube, concrete crushing and/or buckling of the steel I-section occurred.

3.2 Specimens under Concentric Compression

3.2.1 Steel I-section columns

The axial load-strain curves of the two steel I-section columns are shown in Fig. 8, where the axial strains were averaged from readings of the two strain gauges attached at the mid-height of the column. For comparison, the corresponding curve calculated from the stress-strain relationship obtained from flat coupon tests are also plotted in Fig. 8. It can be seen that the two experimental curves agree well with the calculated curve based on the material tests, until an axial strain of around 0.015. After that, the load taken by the steel I-section columns started to decrease because of local buckling of the flanges and web of the section (see Fig. 7a). It is evident that while the steel could still reach its yield stress in the two columns, the ductility of the columns was significantly reduced because of the local buckling.

3.2.2 Hybrid columns without an FRP tube

The key test results of all hybrid columns are summarized in Table 3. Fig. 9 shows readings from the seven axial strain gauges attached on the steel I-section and the concrete surface of specimen C-00-0, respectively (i.e., SGs 1-5, 6, 9 in Fig. 5a). All the axial strain readings agreed well with each other in the initial stage of loading, but those from the two installed on the concrete surface (i.e., SG6 and SG9) started to decrease after an axial strain of around 0.002 and thus deviated from the others, due to the cracking and spalling of concrete. For the same reason, the discrepancies between readings of the five strain gauges (i.e., SGs 1-5) on the steel surface kept increasing after that strain level, although these gauges still recorded increasing axial strains. Similar observations were also noted for specimen S-00-0.

Fig. 10 shows the axial load-axial strain curves of the two specimens without an FRP tube (i.e., specimens C-00-0 and S-00-0), where the axial strains were averaged from readings of the axial strain gauges attached on the embedded steel section. The axial load-axial strain curves of each constituent (i.e., concrete and steel section) and their sum (labeled as “Steel + Concrete”) are also shown in Fig. 10 for comparison; the curve of concrete was obtained

based on the stress-strain curve from standard cylinder (150 mm × 300 mm) tests of concrete. It is evident that the peak loads of specimens C-00-0 and S-00-0 are significantly lower than may be expected from the simple addition of the axial load-axial strain curves of steel and concrete (see also Table 3). This is believed to be due to the lower compressive strengths of concrete in the columns compared to those found from standard cylinder tests. The lower compressive strengths are caused by: (1) the existence of the steel I-section in the column which affects the integrity of concrete; and (2) the larger size of the column compared to standard concrete cylinders (i.e., the size effect) [28,29]. If a reduction factor of 0.6 is applied in calculating the contribution of the concrete following the recommendation by AISC-LRFD [30], the sum of the two materials (i.e., "Steel + 0.6×Concrete" in Fig. 10) is shown to agree much better with the test results of the two columns.

3.2.3 FCSC columns

The axial load-strain curves of the three FCSC specimens under concentric compression are shown in Fig. 11, where the axial strains were averaged from readings of the strain gauges on the steel I-sections, except for specimen S-00-2.5. For specimen S-00-2.5, the axial strains were calculated from the average readings of the two LVDTs measuring the axial shortening of the specimen, as most of the strain gauges on the steel I-section of the specimen were damaged during the test. In Fig. 11, the axial load was normalized by the squash load of the column to eliminate the effect of concrete strength. The squash load is defined by $N_{sq} = f_y A_s + f'_{co} A_c$, where f_y and f'_{co} are the yield stress of steel and cylinder strength of unconfined concrete, respectively, while A_s and A_c are the cross-section areas of the steel I-section and the concrete, respectively.

Fig. 11 shows that the three FCSCs all had an approximately bilinear load-strain curve. It is evident that the ultimate axial strains of the two circular FCSCs are much higher than the buckling strain of the steel I-section. It is also obvious that the two circular FCSCs reached ultimate loads which are significantly higher than the squash load, due to the confinement from the FRP tube. The square FCSC is shown to have a smaller initial slope, although it had a slightly larger cross-section area than the circular FCSCs. This is due to the use of strains calculated from the total axial shortenings (i.e., LVDT readings) in establishing the experimental curves of the square FCSC. The strains from LVDTs are generally larger than those at mid-height in the initial stage of loading as it include other possible deformation of

the loading system.

Fig. 12 shows the distribution of the mid-height hoop strain around the perimeter of the FRP tube (see Fig. 5a for the layout of the strain gauges) at different loading stages. For the circular specimens, the FRP hoop strain distribution was approximately uniform at low loading levels, but became increasingly non-uniform with the increase of load (Figs. 12a and 12b). The non-uniform hoop strain distribution may be attributed to two reasons: (1) the intrinsic non-uniformity of concrete cracking inside [31]; and (2) the existence of an steel I-section whose deformation is not axis-symmetric. It is also evident that the non-uniformity was more pronounced for the specimen with a thinner FRP tube (Fig. 12b). For the square specimen, the hoop strains recorded by strain gauges at the four corners were generally similar, but small differences were also noted due to the non-uniform lateral deformation of concrete inside.

3.3 Specimens under Eccentric Compression

3.3.1 Axial strain distribution

Typical axial strain distributions over the section are shown in Fig. 13, where the horizontal axis represents the distance to the centerline of the specimen and the vertical axis represents the axial strain value. In Fig. 13 and elsewhere in the paper, compressive axial strains are positive while tensile axial strains are negative, unless otherwise specified. The axial strains at the extreme compression and tension edges were obtained from the strain gauges attached on the outer surface of the FRP tube, while the other axial strains were readings from the strain gauges attached on the steel I-section. As shown in Fig. 13, the distribution of axial strains over the section remains approximately linear with the distance from the center of the section, except for some specimens at a high load level (Figs. 13b-13d). For those specimens (e.g., S-25Ma-2.5), the strain gauges at the extreme compression edge typically recorded a much lower value at a high load level than what may be expected from the plane section assumption. This might be due to the wrinkling/buckles on the FRP tube caused by large compressive deformation, which may have led to damage or debonding of the strain gauges on the tube.

3.3.2 Axial load-shortening curves

The axial shortening of the specimens was obtained from the machine output, which recorded the relative movement between the two loading points (see Fig. 6). It is not difficult to understand that the so-obtained axial shortening is generally larger than the axial shortening at the centerline of the specimens because of the bending deformation of the specimen.

Fig. 14 shows the axial load-shortening curves of all specimens. It is evident from Fig. 14 that the curves of the specimens bent about the major axis of the steel I-section all had a bilinear shape with two ascending branches. By contrast, the curves of the specimens bent about the minor axis generally had a descending branch before the final failure by the rupture of FRP. The peak load of the former was also significantly higher than that of the latter for the same column section and load eccentricity. For specimens bent about the same axis (i.e., major axis), Fig. 14 shows that those tested at a larger eccentricity had a lower initial stiffness, a lower slope of the second branch and a lower load capacity. This is easy to understand as the bending moment and bending deformation are both larger for a specimen tested at a larger eccentricity. It can also be found from Fig. 14 that all the specimens bent about the major axis possessed excellent ductility, with the axial shortening reaching about or over 3% of the height before the ultimate state of FRP rupture. The specimens bent about the minor axis, however, were less ductile, with the ultimate axial shortening being around 1.6% of the height for two of the specimens (Fig. 14b and 14c). The apparently superior behavior of the specimens bent about the major axis was due to the much larger bending stiffness/moment resistance of the steel I-section in that direction.

3.3.3 Effect of thickness of FRP tube

The normalized axial load-deformation (i.e., axial shortening and lateral deformation) curves of FCSCs with different FRP tubes are compared in Fig. 15, where the axial load was again normalized by the squash load of the column to eliminate the effect of concrete strength. For Specimen C-50Ma-1.5, only part of the axial load-lateral deflection curve is given in Fig. 15(b) as the rest of the data was accidentally lost.

Fig. 15 shows that, for the specimens that were bent about their major axis, the use of a thicker FRP tube generally led to a larger slope for the second linear ascending portion of the

curves, which also terminate at a larger ultimate load and deformation. For specimens bent about their minor axis, whose curves generally had a descending branch, the load decreased less rapidly after the peak load for the specimens with a thicker FRP tube. This is consistent with previous studies on FRP-confined reinforced concrete columns (e.g., [32,33]).

3.3.4 Hoop strain distribution

Fig. 16 shows the distribution of the mid-height hoop strain around the perimeter of the FRP tube of the eccentrically-loaded specimens at different loading levels. It is evident that the distribution is highly non-uniform mainly because of the existence of an axial strain gradient over the column section, among other factors. As expected, for the circular specimens, the maximum FRP hoop strain is always found at the extreme compression edge of the FRP tube (i.e., SG7 in Figs. 16a-16c) while the minimum FRP hoop strain at the opposite side of the column (i.e., SG 10). For the square specimens, the maximum FRP hoop strain occurred at one of the two rounded corners on the compression side (i.e., SG6 or SG8, see Figs. 16d-16f).

4 THEORETICAL ANALYSIS

4.1 FCSCs under Concentric Compression

4.1.1 Assumptions and stress-strain models

For FCSCs under concentric compression, the axial load-axial strain curves can be predicted with the assumptions that: (1) the buckling of steel I-section in FCSCs is well constrained and does not occur before the rupture of FRP; (2) the axial stress-strain curve of concrete can be predicted by existing stress-strain models for concrete in FRP-confined solid concrete columns without an embedded steel section; (3) the direct contribution of the thin FRP tubes to the axial load can be ignored due to their small axial stiffness.

With assumption (1) above, the axial load taken by the steel I-section in FCSCs is further assumed to remain unchanged when the axial strain of an FCSC specimen exceeds the buckling strain (i.e., around 0.015) of the steel I-section tested alone under compression. In this way, the axial load-strain curve of steel I-section in an FCSC can be found from steel I-section column tests. With assumption (2) above, the axial stress-strain models presented in [34] and [35] are adopted in the present study for FRP-confined concrete in circular and

square columns, respectively. Both of the stress-strain models were developed based on the well regarded original model proposed by Lam and Teng [36]. They share the same expressions for the stress-strain curves, but have different expressions for the strength and ultimate axial strain of concrete. The models can be expressed by the following equations:

$$\sigma_c = \begin{cases} E_c\varepsilon_c - \dfrac{(E_c - E_2)^2}{4 f'_{co}}\varepsilon_c^2 & 0 \le \varepsilon_c < \varepsilon_t \\ f'_{co} + E_2\varepsilon_c & \varepsilon_t \le \varepsilon_c \le \varepsilon_{cu} \end{cases} \tag{1}$$

$$\varepsilon_t = \frac{2 f'_{co}}{E_c - E_2} \tag{2}$$

$$E_2 = \frac{f'_{cc} - f'_{co}}{\varepsilon_{cu}} \tag{3}$$

where ε_c and σ_c are the axial strain and the axial stress respectively; E_c is the elastic modulus of the unconfined concrete; E_2 is the slope of the linear second portion of the stress-strain curve; f'_{co} is the cylinder compressive strength of the unconfined concrete; ε_{cu} is the ultimate axial strain of confined concrete; ε_t is the transitional strain between the parabolic first portion and the linear second portion; and f'_{cc} is the compressive strength of FRP-confined concrete.

For FRP-confined concrete in circular columns, the equations proposed by Teng *et al.* [34] for f'_{cc} and ε_{cu} are:

$$\frac{f'_{cc}}{f'_{co}} = \begin{cases} 1 + 3.5(\rho_K - 0.01)\rho_\varepsilon & \rho_K \ge 0.01 \\ 1 & \rho_K < 0.01 \end{cases} \tag{4}$$

$$\frac{\varepsilon_{cu}}{\varepsilon_{co}} = 1.75 + 6.5\rho_K^{0.8}\rho_\varepsilon^{1.45} \tag{5}$$

where $\rho_K = E_f t_f / (R f'_{co}/\varepsilon_{co})$ is the FRP confinement stiffness ratio, and $\rho_\varepsilon = \varepsilon_{h,rup}/\varepsilon_{co}$ is the strain ratio; E_f is the elastic modulus of FRP composites in the hoop direction; t_f is the thickness of the FRP composites; R is the radius of the circular section; ε_{co} is the axial strain corresponding to f'_{co}; and $\varepsilon_{h,rup}$ is the FRP hoop rupture strain.

For FRP-confined concrete in square columns, the equations proposed by Lam and Teng [35] for f'_{cc} and ε_{cu} are:

$$\frac{f'_{cc}}{f'_{co}} = \begin{cases} 1+3.3k_s\rho_{Ke}\rho_{\varepsilon} & k_s\rho_{Ke}\rho_{\varepsilon} \geq 0.07 \\ 1 & k_s\rho_{Ke}\rho_{\varepsilon} < 0.07 \end{cases} \quad (6)$$

$$\frac{\varepsilon_{cu}}{\varepsilon_{co}} = 1.75+12k_s\rho_{Ke}\rho_{\varepsilon}^{1.45} \quad (7)$$

$$k_s = \frac{A_e}{A_g} = \frac{1 - 2\left(b - 2r\right)^2 / \left(3A_g\right) - \rho_s}{1 - \rho_s} \quad (8)$$

where $\rho_{Ke} = 2E_f t_f / \left(D_e\, f'_{co} / \varepsilon_{co}\right)$ is the effective confinement stiffness ratio for an FRP-confined square section; $D_e = \sqrt{2}b$ is the diameter of the equivalent circular section of the rectangular section; b is the section width; r is the corner radius; k_s is the ratio between the effective confinement area A_e and the gross area of the square section A_g; and ρ_s is the cross sectional area ratio of the longitudinal steel reinforcement.

As the axial strains were not measured in the concrete cylinder tests, in the theoretical analysis of the present study, the following two equations were used to predict the elastic modulus [37] and the axial strain at peak axial stress [38] of the unconfined concrete respectively:

$$E_c = 4730\sqrt{f'_{co}} \quad (f'_{co} \text{ in MPa}) \quad (9)$$

$$\varepsilon_{co} = 0.000937\sqrt[4]{f'_{co}} \quad (f'_{co} \text{ in MPa}) \quad (10)$$

These two equations have been extensively verified in existing studies and they are thus believed to represent the stress-strain behaviour of unconfined concrete with enough accuracy.

4.1.2 Comparison with test results

The predicted and experimental load-strain curves are compared in Fig. 17 for all the concentrically-loaded specimens. In making the predictions, the rupture strains of FRP tube averaged from the hoop strain gauge readings were used.

It is evident from Figs. 17a-17b that the experimental curves of the circular FCSCs agree well with the predictions, suggesting that the presence of an embedded steel I-section does not affect much the behavior of the confined concrete. It should also be noted that in making the prediction, the unconfined concrete strengths from standard cylinder tests were used without

any reduction, further demonstrating the beneficial effect of the FRP confinement. For the square FCSC (i.e., S-00-2.5), the prediction appears to overestimate the slope and the load enhancement of the second branch of the curve. As the steel I-section shows an approximately elastic-perfectly plastic behavior, this overestimation of the overall behavior is mainly due to the overestimation of the stress-strain behavior of confined concrete. This suggests that Lam and Teng's [35] model may need to be improved for more accurate predictions of concrete in square FCSCs. It should however be noted that, even for concrete in an FRP-confined square column without a steel I-section, the accurate predictions are more difficult than in a circular column, due to the larger scatter of test results of FRP-confined concrete in square columns caused by the more complex stress state of concrete [35,39]. For the square columns, the theoretical analysis also significantly overestimates the initial slope because of the use of LVDT readings to establish the experimental curve, as discussed in Section 3.2.3.

4.2 FCSCs under Eccentric Compression

4.2.1 Section analysis

A conventional theoretical model for section analysis (referred to as section analysis for brevity) based on the so-called fiber element approach was developed for FCSCs under eccentric compression. The experimental axial strain distributions follow approximately the plane section assumption, except for some of the strains measured on the FRP tubes (Fig. 13). As the axial stiffness of FRP tubes was small, their direct contribution in the axial direction was ignored in the analysis. For the same reason, the plane section assumption is adopted and any errors are expected to be small. The method of analysis is similar to that presented in [13] for hybrid double-skin tubular columns.

In the section analysis, the column section is equally divided into a desirable number of layers with a thickness of $d\lambda$ parallel to the neutral axis, as shown in Fig. 18, where λ is the distance to the centerline, b_c is the width of a section layer; dA_s is the area of steel in a layer; f_c and f_s are the stresses of concrete and steel respectively. The section analysis starts with specifying a number of strain values ε_c, ranging from zero to the ultimate axial strain of concrete ε_{cu}, to the extreme compression fiber of the section. For each strain value, the location of the neutral axis is determined by the following criteria: the load eccentricity

calculated from the resultant axial load *N* and the resultant bending moment *M* on the section is sufficiently close to the specified load eccentricity (e.g., the experimental value). To consider the variation of load eccentricity due to the lateral deflection of the specimen, the load eccentricity is adjusted at each step based on experimental measurements. In the present study, the column section was equally divided into 50 layers based on a convergence study.

The stress-strain models proposed by Teng *et al*. [34] and Lam and Teng [35] were adopted in the section analysis for concrete, while the stress-strain curve obtained from the tensile coupon tests (Fig. 4) was used for the steel I-section in both compression and tension. Buckling of the steel section was not considered in the analysis.

4.2.2 Comparison with test results

The predicted and experimental load-strain curves are compared in Fig. 19 for the specimens bent about the major axis. The strain values shown are those of the extreme compression edge of the steel I-section at the mid-height (i.e., readings of SG1 and SG2 in Fig. 5a), as the measured axial strains from the surfaces of the FRP tubes appeared to be not reliable as discussed in Section 3.3.

Figs. 19a and 19b show that the predicted load-strain curves generally agree reasonably well with the test results of the circular specimens. The theoretical model, however, tends to underestimate the ultimate axial strain. This is believed to be due to the use of Teng *et al*.'s [34] and Lam and Teng's [35] stress-strain models, which were developed based on results from concentrically-loaded FRP-confined concrete columns. It has been found that the ultimate axial strain of FRP-confined concrete in eccentrically-loaded specimens is generally larger than the counterpart in columns under concentric compression [13,40,41].

Fig. 19c shows that the theoretical model overestimates the test results of the square FCSCs. As Lam and Teng's [35] model was shown to overestimate the stress-strain behavior of concrete in concentrically-loaded square FCSC (see Fig. 17c), it may also be the source of inaccuracy for the section analysis. To clarify this issue, the stress-strain curve of FRP-confined concrete obtained from test results of specimen S-00-2.5 was used in the section analysis instead of Lam and Teng's [35] model, and the predictions are compared with the test results in Fig. 20. With this simple change, the theoretical predictions become much

closer to the test results. Apparently, future research is needed to develop a more reliable stress-strain model for the concrete in square FCSCs.

Fig. 21 shows the comparison for the specimens bent about the minor axis. Again, the strain values are those of the extreme compression edge of the steel I-section at the mid-height. It is evident that the predictions agree reasonably well with the test results.

5 CONCLUSIONS

This paper has presented and interpreted the results of a series of compression tests on FCSCs. The test results of specimens under concentric compression have been compared with the predictions based on existing stress-strain models of concrete in FRP-confined solid concrete columns without a steel I-section. A section analysis based on the plane section assumption and the fiber element approach has also been presented and employed to predict the responses of the columns tested under eccentric compression. Based on the results and discussions presented in the paper, the following conclusions can be drawn:

(1) The buckling of steel I-section was well constrained and the concrete was effectively confined in FCSCs, leading to a very ductile response under both concentric and eccentric compression;
(2) The plain section assumption is generally valid for an FCSC section subjected to eccentric axial compression;
(3) The axial load capacity of FCSCs decreases with the load eccentricity, but the ductility of the column increases with the load eccentricity;
(4) Teng *et al.*'s [34] model predicts well the test results of concrete in circular FCSCs, while further research is needed for an improved stress-strain model for concrete in square FCSCs;
(5) Predictions from the section analysis, with the stress-strain behavior of the confined concrete being appropriately captured, are in reasonably close agreement with the test results.

6 ACKNOWLEDGEMENTS

The authors are grateful for the financial supports received from the Australian Research Council through a *Discovery Early Career Researcher Award* (Project ID: DE140101349) for

the first author. The authors also wish to thank Messrs Khorsand Masoumi and Yuen Chun Ching for their valuable contribution to the experimental work.

7 REFERENCES

[1] Teng JG, Yu T, Wong YL, Dong SL. Hybrid FRP–concrete–steel tubular columns: concept and behavior. Construction and Building Materials 2007;21:846-54.

[2] Hollaway LC, Teng JG. Strengthening and Rehabilitation of Civil Infrastructures Using Fibre-Reinforced Polymer (FRP) Composites: Woodhead Publishing, Cambridge, UK, 2008.

[3] Feng P, Cheng S, Bai Y, Ye L. Mechanical behavior of concrete-filled square steel tube with FRP-confined concrete core subjected to axial compression. Composite structures 2015.

[4] Karimi K, El-Dakhakhni WW, Tait MJ. Performance enhancement of steel columns using concrete-filled composite jackets. Journal of Performance of Constructed Facilities 2011;25:189-201.

[5] Fam AZ, Rizkalla SH. Behavior of axially loaded concrete-filled circular fiber-reinforced polymer tubes. ACI Structural Journal 2001;98:280-9.

[6] Yu T, Teng J. Design of concrete-filled FRP tubular columns: provisions in the Chinese technical code for infrastructure application of FRP composites. Journal of Composites for Construction 2010;15:451-61.

[7] Yu T, Zhang B, Teng JG. Unified cyclic stress–strain model for normal and high strength concrete confined with FRP. Engineering Structures 2015;102:189-201.

[8] Mohamed HM, Masmoudi R. Axial load capacity of concrete-filled FRP tube columns: Experimental versus theoretical predictions. Journal of Composites for Construction 2010;14:231-43.

[9] Mohamed H, Masmoudi R. Compressive behavior of reinforced concrete-filled FRP tubes. ACI Special Publication 2008;257:91-108.

[10] Ozbakkaloglu T, Oehlers DJ. Concrete-Filled Square and Rectangular FRP Tubes under Axial Compression. Journal of Composites for Construction 2008;12:469-77.

[11] Ozbakkaloglu T. Compressive behavior of concrete-filled FRP tube columns: Assessment of critical column parameters. Engineering Structures 2013;51:188-99.

[12] Yu T, Teng JG, Wong YL. Stress-strain behavior of concrete in hybrid FRP-concrete-steel double-skin tubular columns. Journal of Structural Engineering 2010;136:379-89.

[13] Yu T, Wong YL, Teng JG. Behavior of hybrid FRP-concrete-steel double-skin tubular

columns subjected to eccentric compression. Advances in Structural Engineering 2010;13:961-74.
[14] Yu T, Teng JG. Behavior of hybrid FRP-concrete-steel double-skin tubular columns with a square outer tube and a circular inner tube subjected to axial compression. Journal of Composites for Construction 2013;17:271-9.
[15] Ozbakkaloglu T, Idris Y. Seismic behavior of FRP-high-strength concrete–steel double-skin tubular columns. Journal of Structural Engineering 2014;140:04014019.
[16] Zhang B, Teng JG, Yu T. Experimental behavior of hybrid FRP–concrete–steel double-skin tubular columns under combined axial compression and cyclic lateral loading. Engineering Structures 2015;99:214-31.
[17] Xiao. Applications of FRP composites in concrete columns. Advances in Structural Engineering 2004;7:335-43.
[18] Hu YM, Yu T, Teng JG. FRP-confined circular concrete-filled thin steel tubes under axial compression. Journal of Composites for Construction 2011;15:850-60.
[19] Teng JG, Hu YM, Yu T. Stress–strain model for concrete in FRP-confined steel tubular columns. Engineering Structures 2013;49:156-67.
[20] Yu T, Hu Y, Teng JG. FRP-confined circular concrete-filled steel tubular columns under cyclic axial compression. Journal of Constructional Steel Research 2014;94:33-48.
[21] Liu X, Nanni A, Silva P. Rehabilitation of compression steel members using FRP pipes filled with non-expansive and expansive light-weight concrete. Advances in Structural Engineering 2005;8:129-42.
[22] Karimi K, Tait MJ, El-Dakhakhni WW. Testing and modeling of a novel FRP-encased steel-concrete composite column. Composite structures 2011;93:1463-73.
[23] Karimi K, Tait MJ, El-Dakhakhni WW. Influence of slenderness on the behavior of a FRP-encased steel-concrete composite column. Journal of Composites for Construction 2012;16:100-9.
[24] Zakaib S, Fam A. Flexural performance and moment connection of concrete-filled GFRP tube–encased steel I-sections. Journal of Composites for Construction 2012;16:604-13.
[25] AS 1391. Metallic materials - Tensile testing at ambient temperature. Standards Australia: Sydney, NSW, Australia; 2007.
[26] ASTM D3039. Standard Test Method for Tensile Properties of Polymer Matrix Composite Materials. Pennsylvania, USA.: ASTM D3039 / D3039M - 08, ASTM International, West Conshohocken; 2008.
[27] Shahawy M, Mirmiran A, Beitelman T. Tests and modeling of carbon-wrapped concrete

columns. Composites Part B: Engineering 2000;31:471-80.
[28] Wang YF, Wu HL. Size effect of concrete short columns confined with aramid FRP jackets. Journal of Composites for Construction 2011;15:535-44.
[29] Park R, Paulay T. Reinforced Concrete Structures. New York, USA.: Wiley, 1975.
[30] AISC-LRFD. Load and Resistance Factor Design Specification for Structural Steel Building. Chicago: American Institute of Steel Construction; 1999.
[31] Lam L, Teng J. Ultimate condition of fiber reinforced polymer-confined concrete. Journal of Composites for Construction 2004;8:539-48.
[32] Jiang T, Teng JG. Analysis-oriented stress-strain models for FRP-confined concrete. Engineering Structures 2007;29:2968-86.
[33] Samaan M, Mirmiran A, Shahawy M. Model of concrete confined by fiber composites. Journal of Structural Engineering 1998;124:1025-31.
[34] Teng JG, Jiang T, Lam L, Luo YZ. Refinement of a design-oriented stress-strain model for FRP-confined concrete. Journal of Composites for Construction 2009;13:269-78.
[35] Lam L, Teng JG. Design-oriented stress-strain model for FRP-confined concrete in rectangular columns. Journal of Reinforced Plastics and Composites 2003;22:1149-86.
[36] Lam L, Teng JG. Design-oriented stress-strain model for FRP-confined concrete. Construction and Building Materials 2003;17:471-89.
[37] ACI 318-08. Building Code Requirements for Structural Concrete and Commentary. American Concrete Institute, Farmington Hills, Michigan, USA; 2008.
[38] Popovics S. A numerical approach to the complete stress-strain curve of concrete. Cement and concrete research 1973;3:583-99.
[39] Lin G, Teng JG. FRP-confined concrete in square columns: an advanced stress-strain model based on a new approach, In: Proceedings of 4th Asia-Pacific Conference on FRP in Structures (APFIS 2013), 11-13 December, Melbourne, Australia; 2013.
[40] Bisby L, Ranger M. Axial-flexural interaction in circular FRP-confined reinforced concrete columns. Construction and Building Materials 2010;24:1672-81.
[41] Wu YF, Jiang C. Effect of load eccentricity on the stress-strain relationship of FRP-confined concrete columns. Composite structures 2013;98:228-41.

Table 1. Details of circular specimens

Specimen	Batch	Diameter of concrete section (mm)	Specimen height (mm)	Concrete cylinder strength (MPa)	Load eccentricity (mm)	GFRP tube thickness (mm)
C-00-0	Batch 1	203	400	24.9	0	0
C-00-3.0	Batch 1	203	400	24.9	0	3.0
C-00-1.5	Batch 2	203	600	38.0	0	1.5
C-25Ma-3.0	Batch 1	203	600	24.9	25	3.0
C-50Ma-3.0	Batch 1	203	600	24.9	50	3.0
C-25Mi-3.0	Batch 1	203	600	24.9	25	3.0
C-25Ma-1.5	Batch 2	203	600	38.0	25	1.5
C-50Ma-1.5	Batch 2	203	600	38.0	50	1.5
C-25Mi-1.5	Batch 2	203	600	38.0	25	1.5

Table 2. Details of square specimens

Specimen	Batch	Width of concrete section (mm)	Specimen height (mm)	Corner radius (mm)	Concrete cylinder strength (MPa)	Load eccentricity (mm)	GFRP tube thickness (mm)
S-00-0	Batch 1	200	400	25	24.9	0	0
S-00-2.5	Batch 1	200	400	25	24.9	0	2.5
S-25Ma-2.5	Batch 1	200	600	25	24.9	25	2.5
S-50Ma-2.5	Batch 1	200	600	25	24.9	50	2.5
S-25Mi-2.5	Batch 1	200	600	25	24.9	25	2.5

Table 3. Key test results

Specimen	N_p **(kN)**	N_u **(kN)**	$\Delta_{a,p}$ **(mm)**	$\Delta_{a,u}$ **(mm)**	N_{co} **(kN)**	N_s **(kN)**	$\frac{N_p}{N_{co}+N_s}$
C-00-0	1245.0	N.A.	2.44	N.A.	750.9	774.0	0.82
C-00-3.0	3215.6	3215.6	18.59	18.59			2.11
C-00-1.5	2809.5	2809.5	19.18	19.18	1146.0		1.46
C-25Ma-3.0	1767.5	1767.5	22.52	22.52	750.9		1.16
C-50Ma-3.0	1069.5	1069.5	23.68	23.68			0.70
C-25Mi-3.0	1103.9	967.2	5.43	16.22			0.72
C-25Ma-1.5	1811.1	1811.1	18.48	18.48	1146.0		0.94
C-50Ma-1.5	1200.8	1200.8	19.42	19.42			0.63
C-25Mi-1.5	1140.2	902.4	3.92	8.51			0.59
S-00-0	1404.7	N.A.	2.89	N.A.	927.7		0.83
S-00-2.5	1734.2	1734.2	6.79	6.79			1.02
S-25Ma-2.5	1372.3	1372.3	15.59	15.59			0.81
S-50Mi-2.5	1028.0	1028.0	19.41	19.41			0.60
S-25Mi-2.5	1078.8	674.3	3.21	8.52			0.63

Note: N_p - Peak axial load; N_u - Axial load at FRP rupture; $\Delta_{a,p}$ - Axial shortening at peak axial load; $\Delta_{a,u}$ - Axial shortening at FRP rupture; N_{co} - Unconfined concrete strength times the area of the concrete section; N_s - Ultimate load of the steel I-section; N.A. - Not applicable.

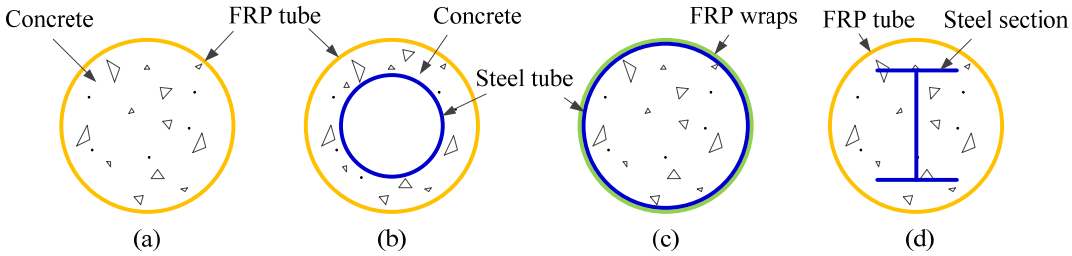

Fig. 1 Typical cross-sections of hybrid FRP tubular columns:
(a) CFFT; (b) DSTC; (c) CCFT; (d) FCSC

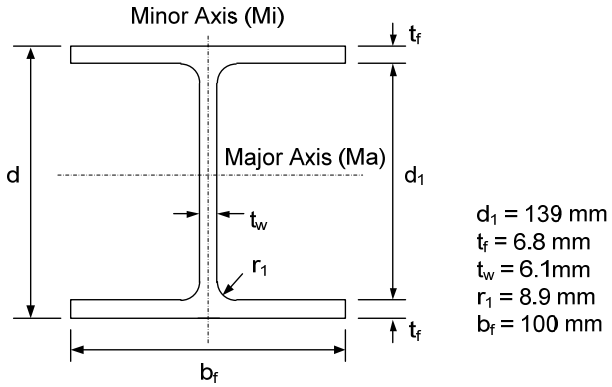

Fig. 2 Dimensions of steel I-section

(a) Locating steel I-section (b) Concrete casting

(c) End strengthening with CFRP strips (d) End surface capping

Fig. 3 Specimen preparation

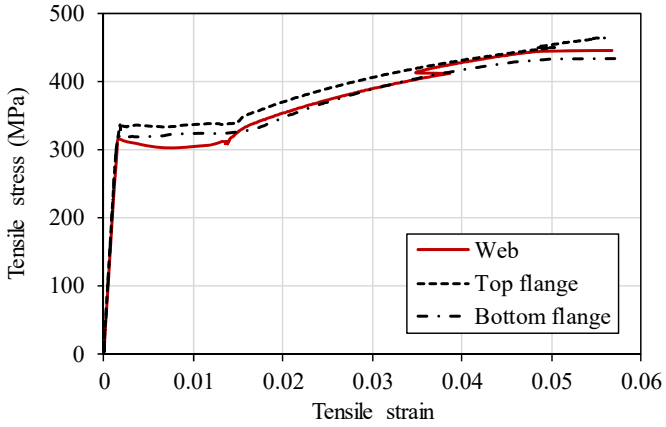

Fig. 4 Tensile stress-strain curves of steel coupons cut at different locations

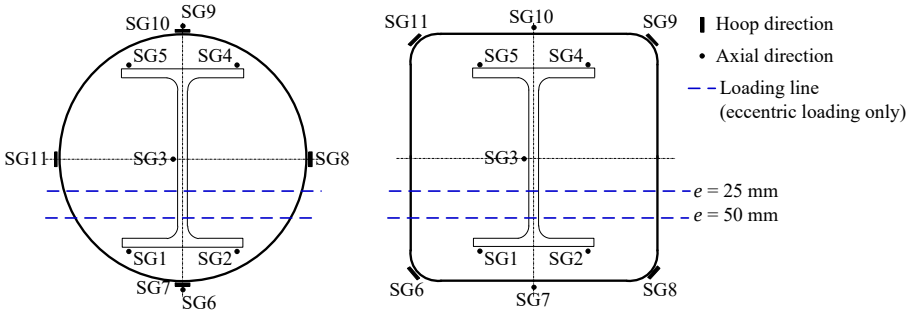

(a) Concentric loading and bending about major axis

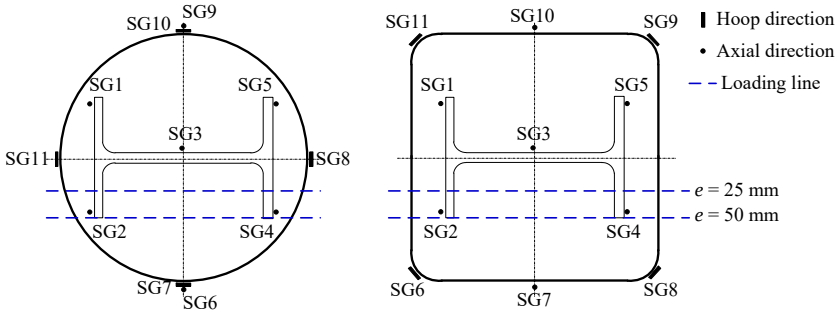

(b) Bending about minor axis

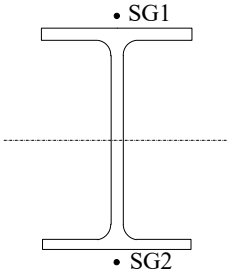

(c) Bare steel I-section

Fig. 5 Layout of strain gauges

(a) Specimen during test

(b) Bottom end

Fig. 6 Set-up for eccentric compression test

(a) Steel I-section

(b) Specimen C-00-0

(c) Specimen C-00-3.0

(d) Specimen S-00-2.5

(e) Specimen C-25Ma-3.0

(f) Specimen S-25Ma-2.5

Fig. 7 Typical specimens after test

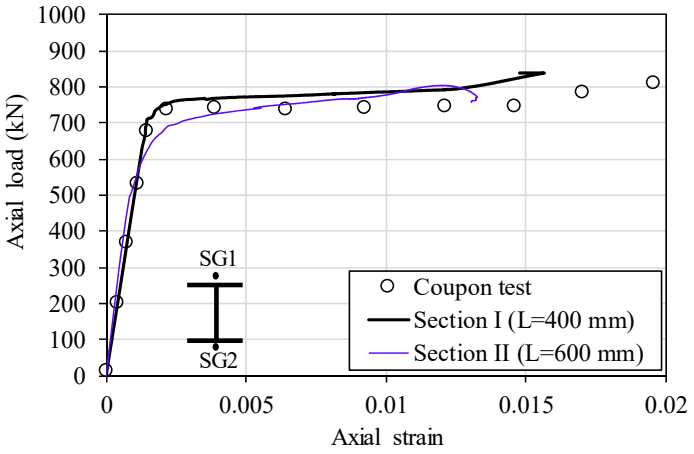

Fig. 8 Axial load-axial strain curves of steel I-sections

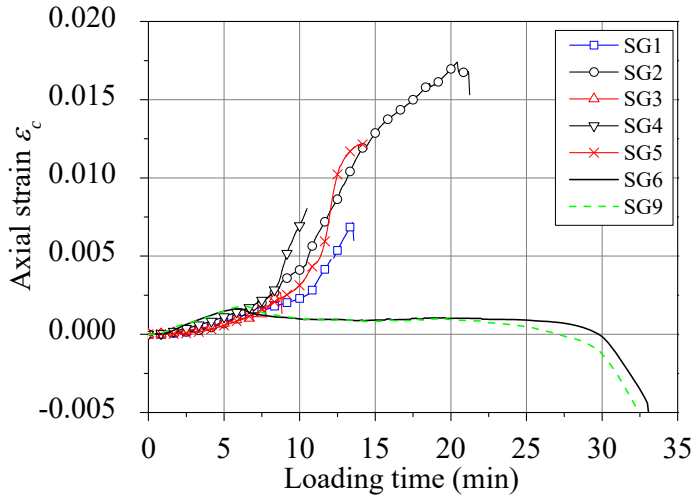

Fig. 9 Readings of strain gauges at different locations of Specimen C-00-0

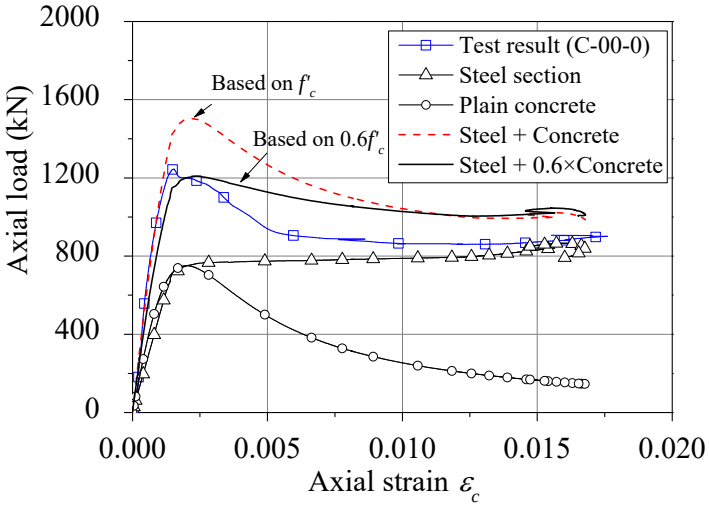

(a) Circular specimen (C-00-0)

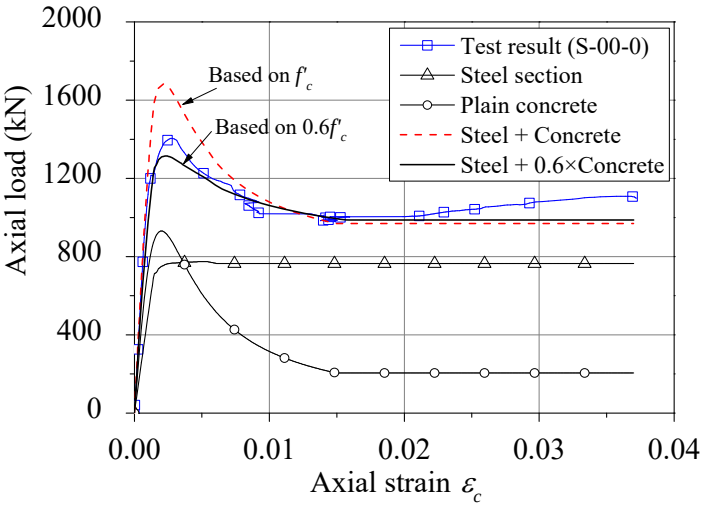

(b) Square specimen (S-00-0)

Fig. 10 Axial load-axial strain curves of specimens under concentric compression

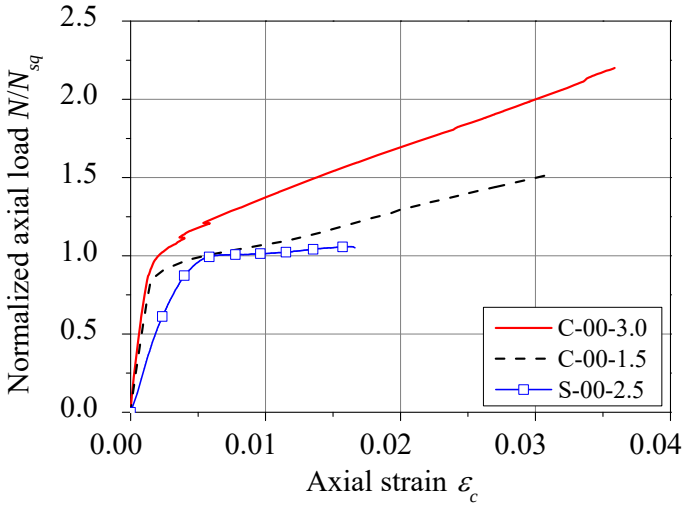

Fig. 11 Normalized axial load-axial strain curves of FCSCs under concentric compression

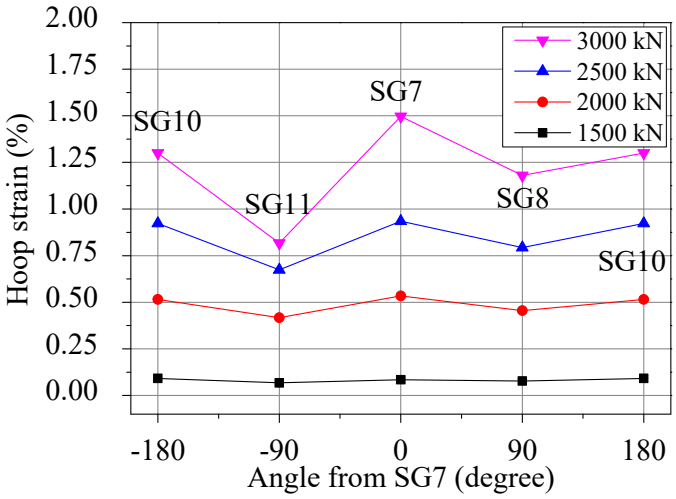

(a) C-00-3.0

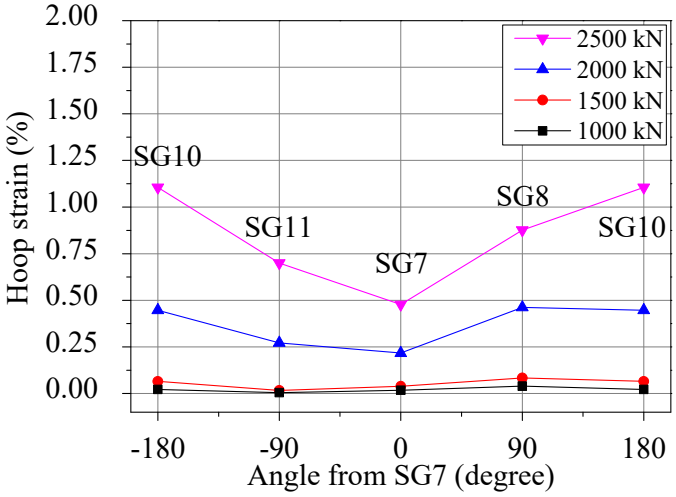

(b) C-00-1.5

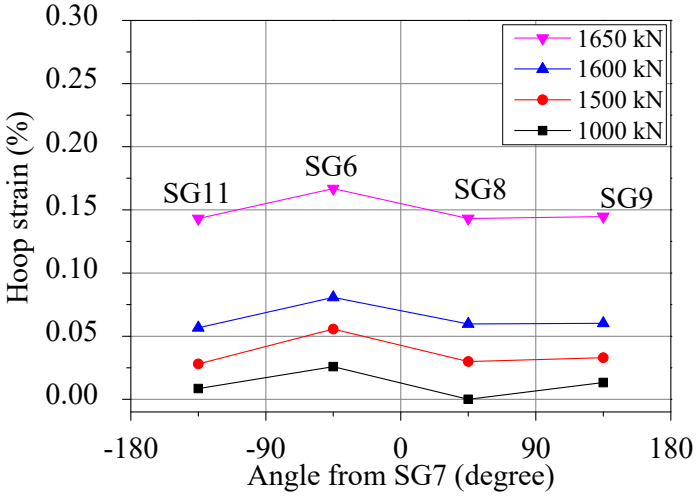

(c) S-00-2.5

Fig. 12 Hoop strain distribution of specimens under concentric compression

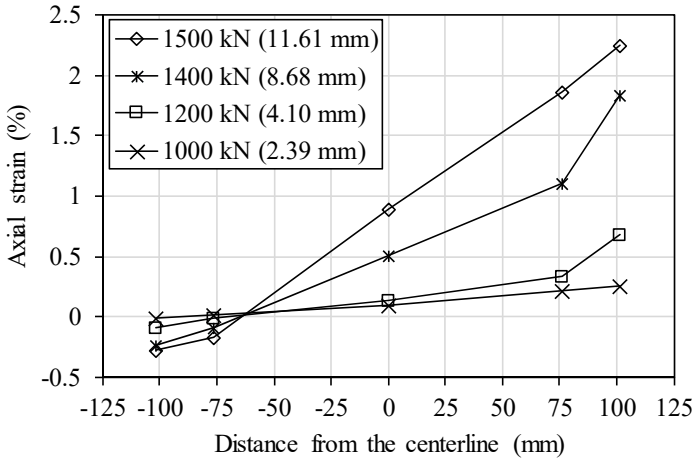

(a) C-25Ma-3.0

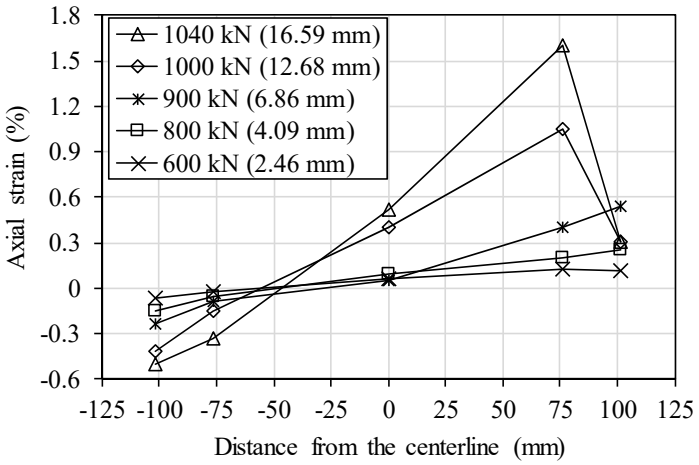

(b) C-50Ma-3.0

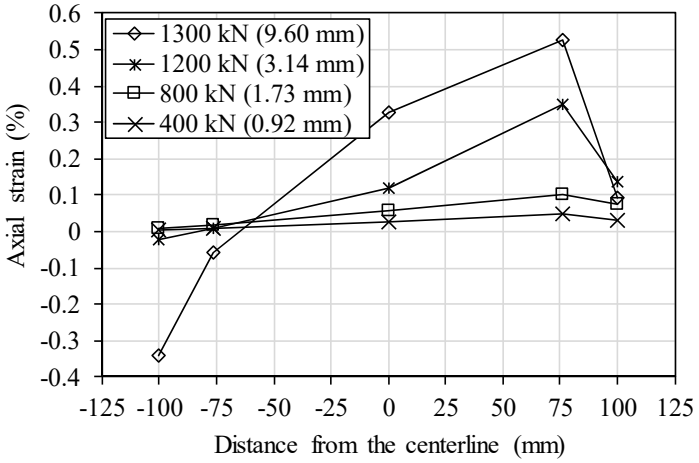

(c) S-25Ma-2.5

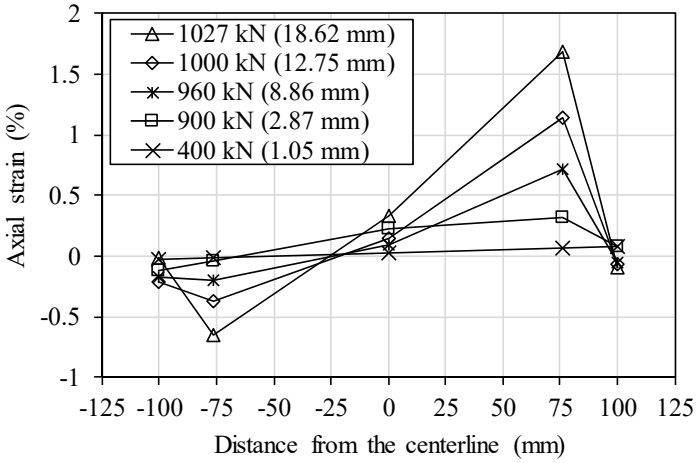

(d) S-50Ma-2.5

Fig. 13 Axial strain distributions over the section

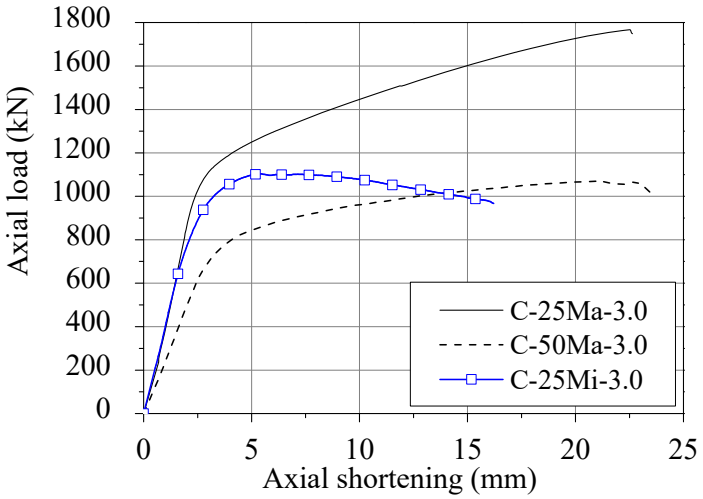

(a) Circular specimens, $t_f = 3.0$ mm

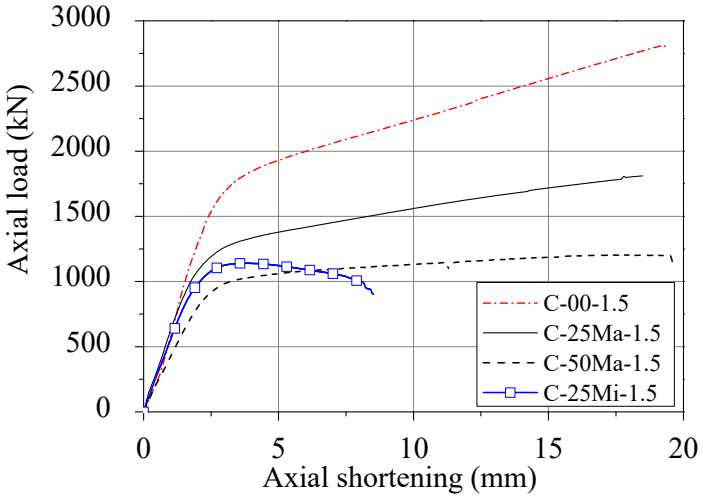

(b) Circular specimens, $t_f = 1.5$ mm

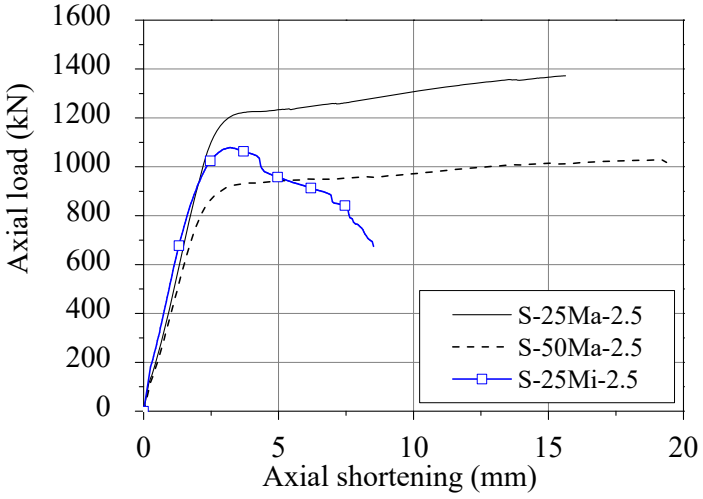

(c) Square specimens

Fig. 14 Axial load-axial shortening curves of specimens under eccentric compression

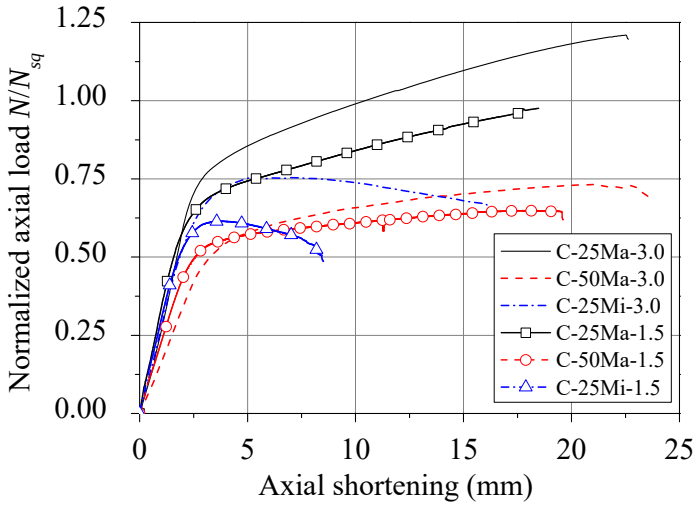

(a) Normalized axial load-axial shortening curves

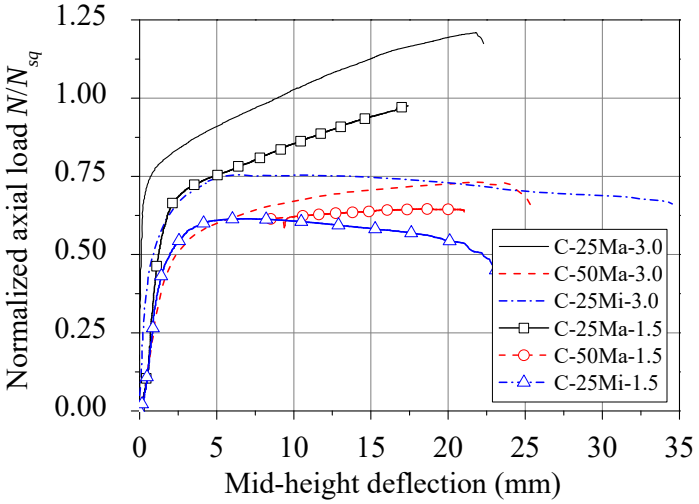

(b) Normalized axial load-lateral deflection curves

Fig. 15 Effect of thickness of FRP tube

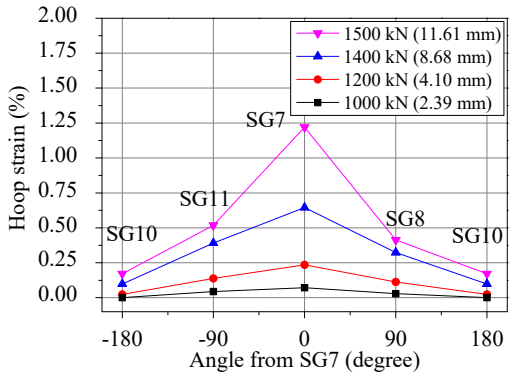

(a) C-25Ma-3.0

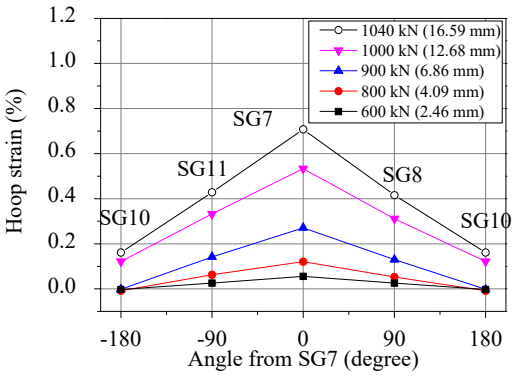

(b) C-50Ma-3.0

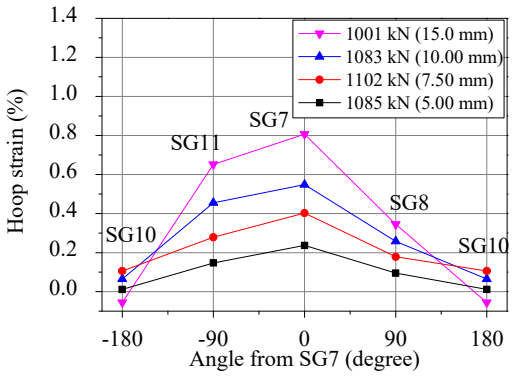

(c) C-25Mi-3.0

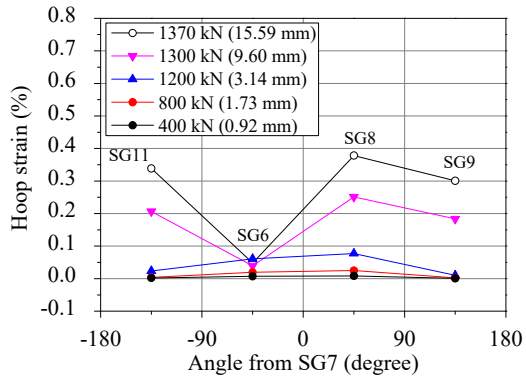

(d) S-25Ma-2.5

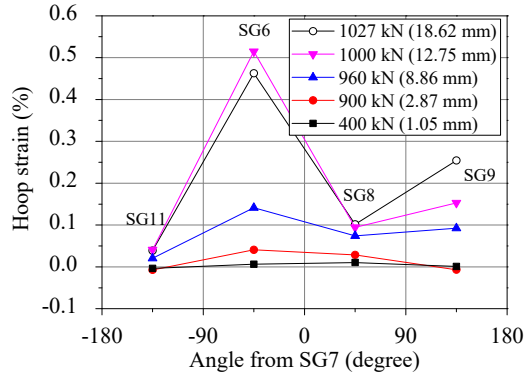

(e) S-50Ma-2.5

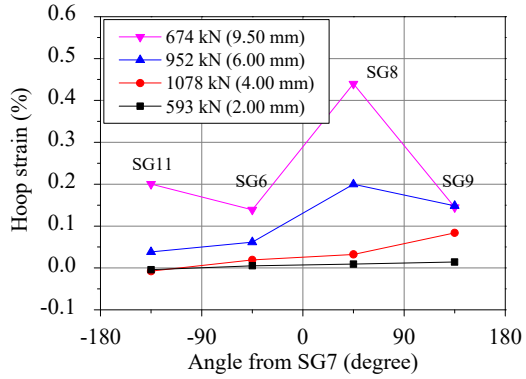

(f) S-25Mi-2.5

Fig. 16 Hoop strain distribution of specimens under eccentric compression

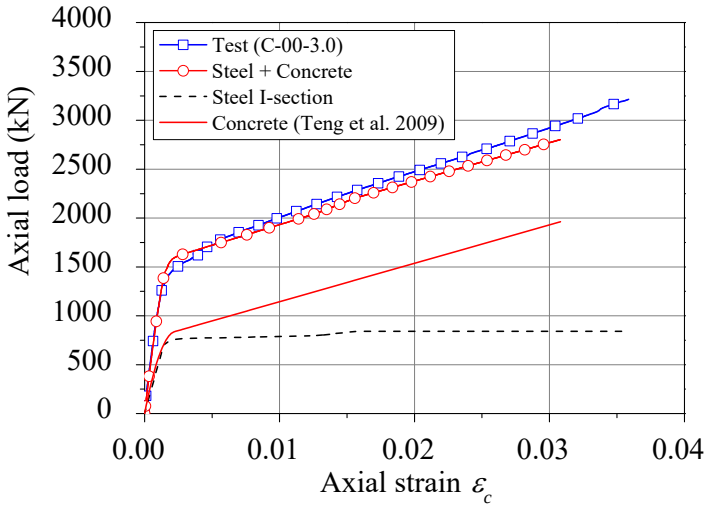

(a) Specimen C-00-3.0

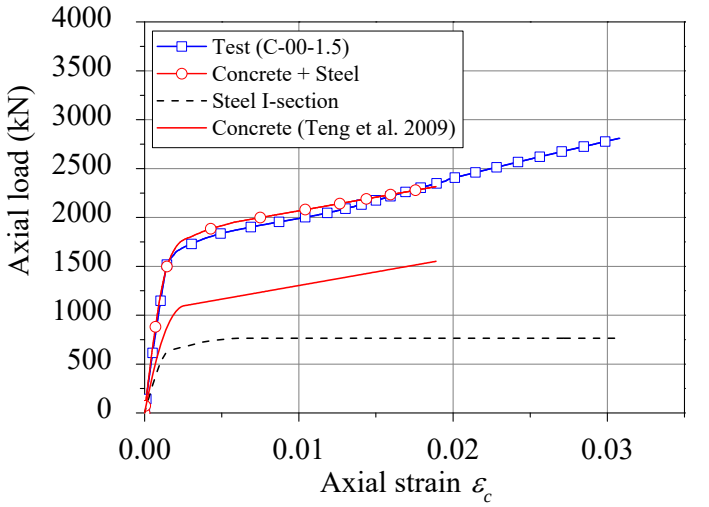

(b) Specimen C-00-1.5

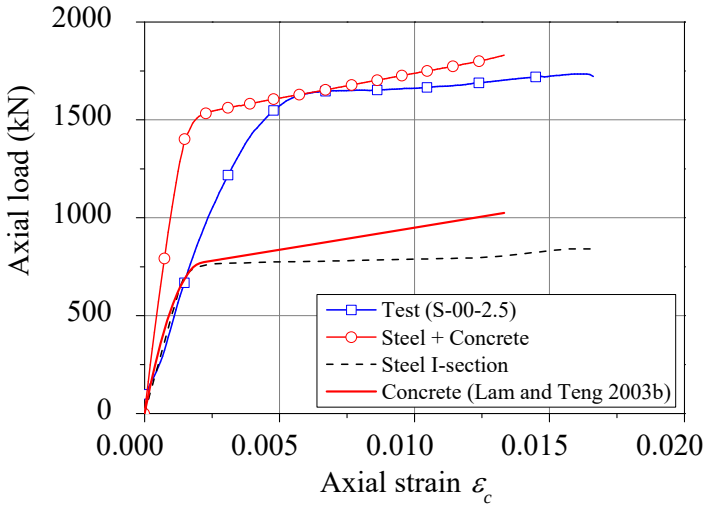

(c) Specimen S-00-2.5

Fig. 17 Comparison between experimental and theoretical results for FCSCs under concentric compression

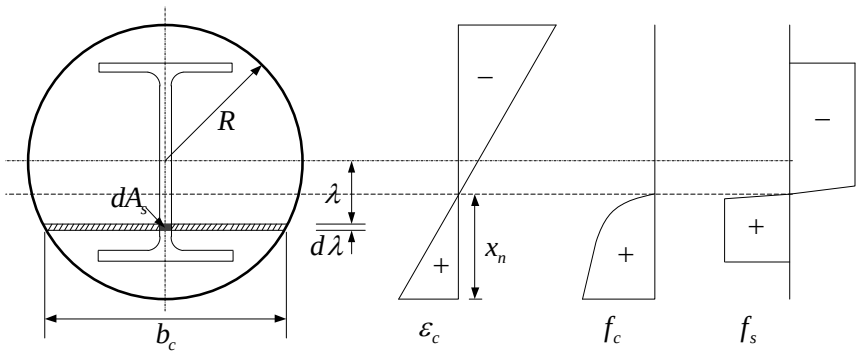

Fig. 18 Strains and stresses over an FCSC circular section bent about the major axis of the steel I-section

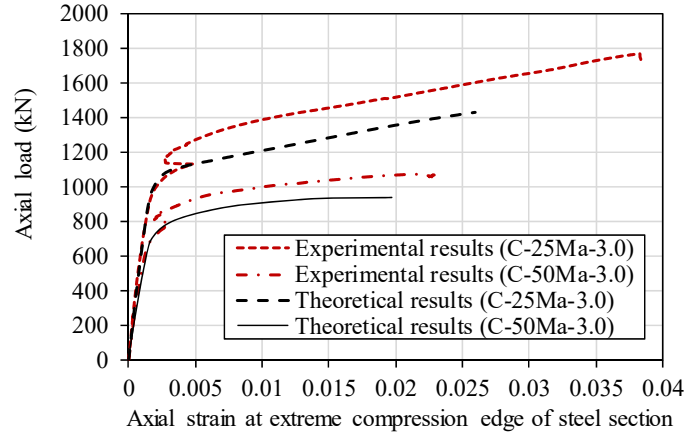

(a) Circular specimens, $t_f = 3.0$ mm

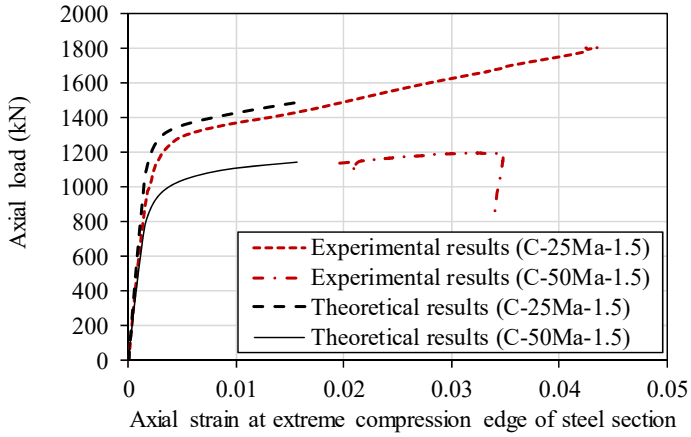

(b) Circular specimens, $t_f = 1.5$ mm

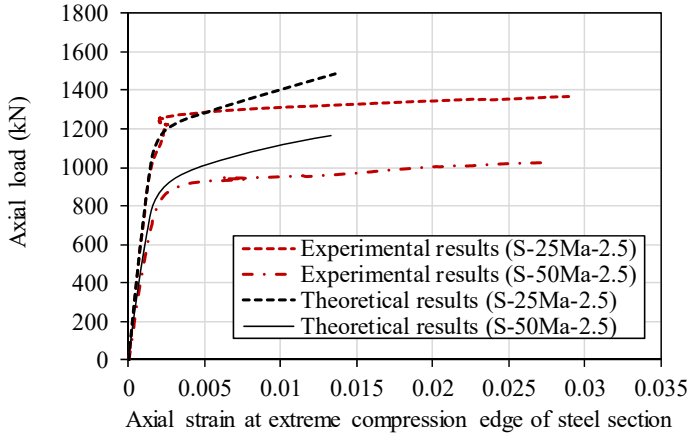

(c) Square specimens

Fig. 19 Comparison between experimental and theoretical results for FCSCs bent about the major axis

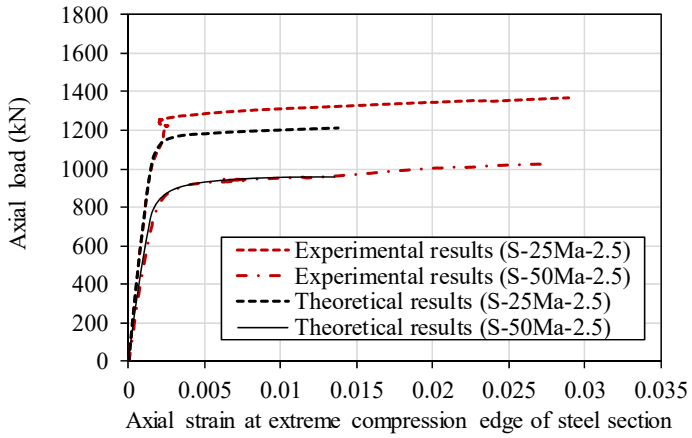

Fig. 20 Comparison between experimental and theoretical results for square FCSCs using experimental stress-strain curve of FRP-confined concrete

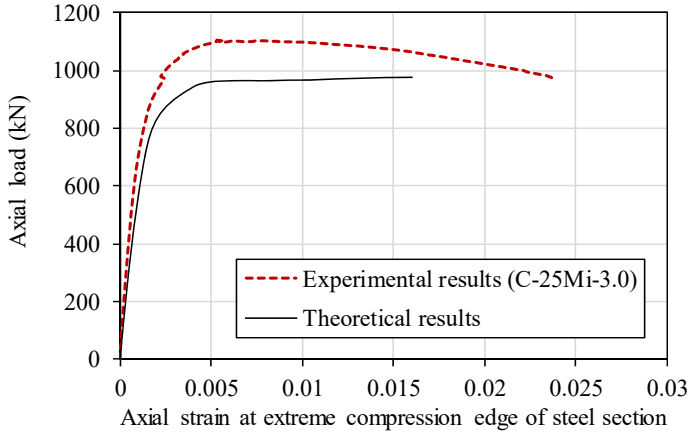

(a) C-25Mi-3.0

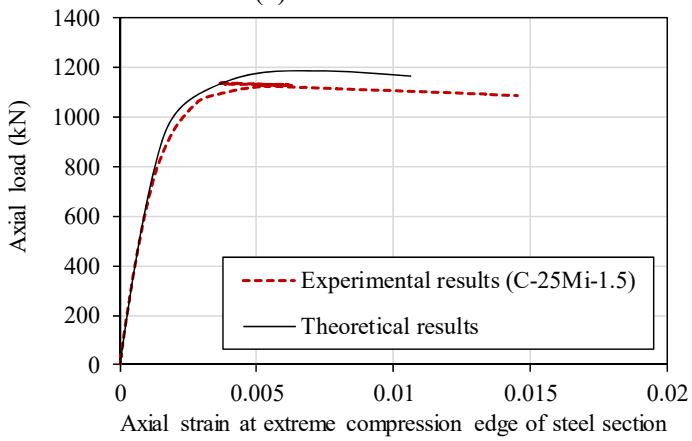

(b) C-25Mi-1.5

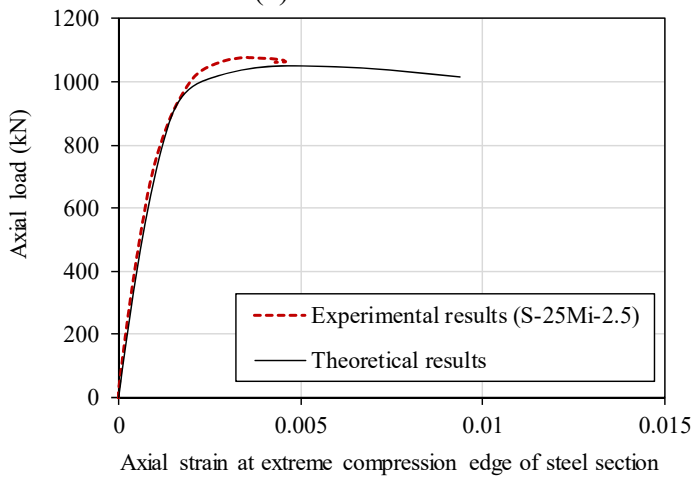

(c) S-25Mi-2.5

Fig. 21 Comparison between experimental and theoretical results for specimens bent about the minor axis